SOLUTION OF SHALLOW WATER EQUATIONS FOR COMPLEX FLOW DOMAINS VIA BOUNDARY-FITTED CO-ORDINATES

J. HAEUSER, H.-G. PAAP, D. EPPEL AND A. MUELLER

Institute of Physics, GKSS-Research Center, 2054 Geesthacht, Germany

SUMMARY

Many problems of applied oceanography and environmental science demand the solution of the momentum, mass and energy equations on physical domains having curving coastlines. Finite-difference calculations representing the boundary as a step function may give inaccurate results near the coastline where simulation results are of greatest interest for numerous applications. This suggests the use of methods which are capable of handling the problem of boundary curvature.

This paper presents computational results for the shallow water equations on a circular ring of constant depth, employing the concept of boundary fitted grids (BFG) for an accurate representation of the boundary. All calculations are performed on a rectangle in the transformed plane using a mesh with square grid spacing. Comparisons of the simulations of transient normal mode oscillations and analytic solutions are shown, demonstrating that this technique yields accurate results in situations (provided that there is a reasonable choice of grid) involving a curved boundary. The software developed allows application to any two-dimensional area, regardless of the complexity of the geometry.

Simulation runs were made with two co-ordinate systems. For the first system, the grid point distribution was obtained from polar co-ordinates. For the second one, grid point positions were calculated numerically, solving Poisson's equation. It was found that small variations in the metric coefficients do not deteriorate the accuracy of the simulation results.

Moreover, comparisons of surface elevation and velocity components at grid points near the inner and outer radii obtained from an x–y Cartesian grid model with the BFG simulation were made. The former model produced inaccuracies at grid points near boundaries, and, owing to the large number of mesh points used to yield the necessary fine resolution, the computation time was found to be a factor of three higher.

KEY WORDS   Shallow Water Equations   Boundary Fitted Grids   Comparison of Boundary Fitted Grid Model with x–y Cartesian Grid Model   Annular Ring Solutions

INTRODUCTION

Many problems of mathematical physics demand the solution of partial differential equations. In most cases analytic solutions cannot be obtained; thus one has to resort to numerical solutions. Very often the numerical solution of a problem is aggravated not only by complex physical processes but also by the irregularity of the solution domain. The present paper is concerned with solutions of the shallow water equations (SWE) which describe the free surface and velocity field of a liquid subjected to the gravity field of the earth. The equations serve as an example of the Navier–Stokes equations, which are the basic equations for solving the flow field in tidal rivers, bays and estuaries, and also in atmospheric models.

In recent years numerous simulation models have been applied to problems in oceanography and environmental science, especially to the modelling of pollution in waters and the atmosphere. Many of these problems involve the incorporation of curving coastlines, islands or complicated

bottom topography while the solution is most needed near the boundaries (e.g. storm surge modelling, modelling of thermal plumes in tidal rivers, harbour modelling etc.). In particular, when the flow field and pollutant dispersal in harbour areas are simulated (e.g. the harbours of Bremen or Hamburg), methods are necessary to efficiently describe these complicated regions without the use of an excessive number of grid points, which is demanded by Cartesian models.

Another important group of problems requiring curved boundaries are free surface problems, including the breaking of waves.

The long used technique of approximating boundaries in a step fashion is not adequate for these problems,[1] and simulation models should be improved to reflect the advances in numerical grid generation. This technique becomes even more important for three-dimensional problems of irregular geometry.

During the last decade substantial progress has been made in the solution of PDEs for curved boundaries, mainly due to the introduction of finite element methods,[2-6] the irregular grid finite-difference techniques by Thacker[7,8] and the use of transformation methods, in particular the work of Thompson *et al.*[9-12] Using Thompson's method, where the solution domain is mapped onto a rectangle in the computational plane, the curvilinear co-ordinate system is constructed by elliptic differential operators (a Poisson equation is used for each curvilinear co-ordinate where the right-hand side of the equation is used for grid line control).[13] All calculations are performed in the transformed plane. Since the solution area in this plane is a rectangle, the problem is reduced to the solution of the transformed equations on this rectangle, which is an advantage in comparison to the original problem, and substantially facilitates the computer programming. The metric coefficients, needed for the transformed equations, are calculated numerically from the resulting grid point distribution. This distribution can be obtained, for instance, from Thompson's TOMCAT code or from the improved version, WESCOR by Johnson and Thompson[14] where a multi-connected region is mapped onto a multi-connected region.

If, however, the solution area is very complex the mapping on a single rectangle often does not yield the desired grid line configuration; for instance if flow past a cylinder (2D) is considered, the mapping of the boundary of the doubly-connected solution area on the boundary of a single rectangle cannot result in a gridline pattern which resembles the pattern of the streamlines. The important idea for the solution of these problems is the use of composite grids, as implemented in the code of Coleman.[15] The domain of interest is subdivided into a set of connected charts (also called segments), which cover the physical area, forming a so-called atlas. Each chart then is mapped onto a rectangle (2D) or onto a box (3D). A 2D example is given in Figure 1.

Either of the above mentioned codes can be used for the solution of the shallow water equations on an annular sheet of water bounded by concentric circles. For this problem an analytic solution exists, and the influence of slightly varying metric coefficients on the solution can be investigated. So far not much attention has been given to the numerical errors induced by the co-ordinate system and the transformation itself, since variable coefficients occur in the transformed equations. Two recently published papers by Mastin[16] and Kerlick and Kloper[17] deal with this subject.

The numerical solution involves two spatially staggered grids, one for the velocity components and the other for the surface elevation. Computations are initialized to normal modes of the basin and carried forward for a time approximately equal to fifty cycles of the normal mode.

The subject of this paper is not grid generation, rather it is assumed that all metric coefficients, which occur in the transformed SWEs are known at each grid point. The emphasis of this presentation is on the solution of the transformed SWEs on complex solution domains, using a specified grid point distribution. Although the example presented is for an annular ring, the generation of the computational grid for more complicated geometries, as in Figure 1, does not
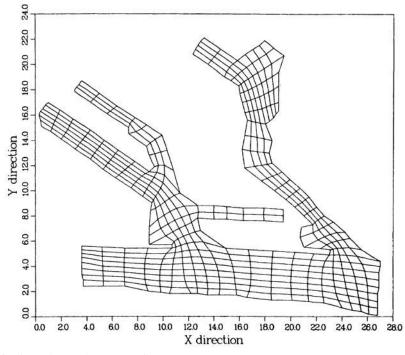
Figure 1. This plot shows that much more complicated areas than the annular ring can be handled by boundary conformed co-ordinate systems. The solution domain shown is a part of the Hamburg Harbour area. The grid line distribution was generated using Coleman's idea of segmentation,[15] demonstrating the capability of modelling regions with many segments. The solution domain is subdivided into a set of contiguous segments which are mapped onto rectangles. The transformed PDEs are then solved on these rectangles. Local refinement of the grid is easily possible on each segment

pose any problem. If non-adaptive grids are used, grid generation and solution of governing equations are completely decoupled.

SHALLOW WATER EQUATIONS

We start with the linearized SWEs, that is, we assume small oscillations, i.e. $h \ll H$ (see Figure 2).

$$\frac{\partial u}{\partial t} + g\frac{\partial h}{\partial x} - fv = 0, \tag{1}$$

$$\frac{\partial v}{\partial t} + g\frac{\partial h}{\partial y} + fu = 0, \tag{2}$$

$$\frac{\partial h}{\partial t} + H\frac{\partial u}{\partial x} + H\frac{\partial v}{\partial y} = 0, \tag{3}$$

where u and v have the dimensions of velocity, f denotes the Coriolis force and H is the constant still water depth $(D = H)$.

The above equations describe linear long waves in an inviscid rotating ocean. The Coriolis force is of the form $\mathbf{f} \times \mathbf{u}$ where $\mathbf{f}$ points in the direction of the axis of rotation. Equations (1)–(3) are solved for an annular sheet of water bounded by concentric circles. This problem has an analytic solution.[18] For the concentric circles to represent solid walls, it is required that
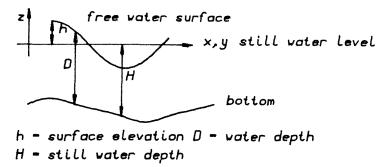
Figure 2. Co-ordinate system: h = surface elevation, D = water depth, H = still water depth

components of the velocity normal to these walls vanish. For the analytic solution harmonic time dependence is assumed. In the following u, v and h depend only on spatial co-ordinates r, θ but may be complex quantities. The final solution is obtained by multiplication with $\exp(i\omega t)$ and taking the real part. For harmonic time dependence, the spatial part of the SWEs takes the form

$$u = \frac{g}{\omega^2 - f^2}\left(\frac{\partial h}{\partial r}(i\omega \cos \theta + f \sin \theta) - \frac{1}{r}\frac{\partial h}{\partial \theta}(i\omega \sin \theta - f \cos \theta)\right), \tag{4}$$

$$v = \frac{g}{\omega^2 - f^2}\left(\frac{\partial h}{\partial r}(i\omega \sin \theta - f \cos \theta) + \frac{1}{r}\frac{\partial h}{\partial \theta}(i\omega \cos \theta + f \sin \theta)\right), \tag{5}$$

$$\frac{\partial^2 h}{\partial r^2} + \frac{1}{r}\frac{\partial h}{\partial r} + \frac{1}{r^2}\frac{\partial^2 h}{\partial \theta^2} + \frac{\omega^2 - f^2}{gH}h = 0. \tag{6}$$

For f equal to zero, we have $\partial h/\partial r = 0$ (see equation (20)) and hence contour lines for surface elevation must be perpendicular to the boundaries. Using a separation ansatz in the spatial co-ordinates, $h = R(r)\Phi(\theta)$, the solution of (6) is described by (the most general solution would be a linear combination of Bessel and Neumann functions, but Neumann functions can be avoided, see below)

$$h(r, \theta, t) = h_0 J_n(kr)\cos(\omega t + n\theta). \tag{7}$$

Rotating the co-ordinate system by an angle θ, and using equations (4) and (5), the normal velocity component $u_{\bar{n}}$ is computed. The vanishing of this component leads to a condition for h, and when the solution for h, equation (7), is inserted, the boundary condition takes the form

$$k_m r_c J'_n(k_m r_c) + \frac{fn}{\omega} J_n(k_m r_c) = 0, \tag{8}$$

where $k_m r_c (m = 1, 2, \ldots)$ denote the set of values satisfying the boundary condition, r_c is the radius of the inner or outer circle, and prime denotes differentiation with respect to the product kr. Insertion of the Bessel function of order n, J_n, into equation (6) leads to the well known dispersion relation:

$$\omega^2 = gHk^2 + f^2. \tag{9}$$

The integers n, m identify the normal mode where n is the number of radial nodes (i.e. nodes or zeros along a given value r = constant) and m describes the number of concentric circles where (i.e. in the radial direction) the elevation is zero. For $f = 0$, one simply has the boundary condition $J'_n(kr) = 0$.

We choose $k_m = 1$ and $r_c = r_1$ (inner radius), $r_c = r_2$ (outer radius) such that equation (8) is satisfied. The dispersion relation then determines the frequency. With this choice for the description of the radial dependence, $R(r)$, Neumann functions are not necessary. Only for $n = 0$ or $f = 0$ is the solution described by standing waves. For arbitrary f, the solution is described by progressive waves, (7).

TRANSFORMATION OF THE SHALLOW WATER EQUATIONS TO CURVILINEAR CO-ORDINATE SYSTEMS

Since the irregularly shaped solution area in the physical plane (x, y) is mapped onto a rectangle in the transformed plane (ξ, η), the governing equations must be transformed too. In general, the transformed equations have variable coefficients, but the solution area has been reduced to a rectangle, spanned by an equidistant mesh. The solution of the transformed equations on a rectangle, however, is much easier than the original problem. Boundary conditions have also to be transformed.

Transforming first derivatives, one can obtain a non-conservative or conservative form. It was found that a conservative form leads to larger numerical error if second derivatives are numerically not interchangeable (see Figure 8). Hence the non-conservative form was used for our calculations:

$$h_x = -\frac{1}{\sqrt{g}}(h_\eta y_\xi - h_\xi y_\eta), \tag{10}$$

$$h_y = -\frac{1}{\sqrt{g}}(h_\xi x_\eta - h_\eta x_\xi). \tag{11}$$

Using equations (10)- and (11) the transformed SWEs read

$$\frac{\partial h}{\partial t} + \frac{1}{\sqrt{g}}(Hu_\xi y_\eta - Hv_\xi x_\eta + Hv_\eta x_\xi - Hu_\eta y_\xi) = 0, \tag{12}$$

$$\frac{\partial (uH)}{\partial t} + \frac{gH}{\sqrt{g}}(h_\xi y_\eta - h_\eta y_\xi) - fvH = 0, \tag{13}$$

$$\frac{\partial (vH)}{\partial t} + \frac{gH}{\sqrt{g}}(h_\eta x_\xi - h_\xi x_\eta) + fuH = 0, \tag{14}$$

where $\sqrt{g}$ is the square root of the determinant of the metric tensor (not to be confused with g which is the acceleration due to the earth is gravity). Recalling the definition of the metric coefficients for co-ordinates $x^m = x^m(\xi^j)$,

$$g_{ik} = \frac{dx^m}{d\xi^i}\frac{dx^m}{d\xi^k}, \tag{15}$$

we find the relationship between the metric coefficients g_{ik} and the partial derivatives $dx^m/d\xi^k$. In our case, we obtain

$$g_{11} = x_\xi^2 + y_\xi^2, \quad g_{22} = x_\eta^2 + y_\eta^2,$$
$$g_{12} = g_{21} = x_\xi x_\eta + y_\xi y_\eta. \tag{16}$$

For the example of the annular ring (polar co-ordinates), the metric coefficients can be determined analytically, that is

$$g_{11} = 1; \quad g_{12} = g_{21} = 0; \quad g_{22} = r^2; \quad \sqrt{g} = r. \tag{17}$$

On the boundary, we separate the velocity into tangential and normal components:

$$\frac{\partial u_{\hat{n}}}{\partial t} + g\frac{\partial h}{\partial \hat{n}} - fu_{\hat{t}} = 0, \tag{18}$$

$$\frac{\partial u_{\hat{t}}}{\partial t} + g\frac{\partial h}{\partial \hat{t}} + fu_{\hat{n}} = 0. \tag{19}$$

As $u_{\hat{n}} = 0$, we obtain from equations (18) and (19)

$$g\frac{\partial h}{\partial \hat{n}} - fu_{\hat{t}} = 0, \tag{20}$$

$$g\frac{\partial h}{\partial \hat{t}} + \frac{\partial u_{\hat{t}}}{\partial t} = 0. \tag{21}$$

Equation (21) determines the tangential velocity, whereas equation (18) could be used to compute the surface elevation h at the boundary. Since in the discrete approximation no h-grid points lie on solid boundaries, this expression is not needed. Neglecting the Coriolis force, equation (20) shows that all contour lines for h must be perpendicular to solid boundaries.

If the boundary of the solution area is described by a curve in parameter representation (e.g. spline), $\mathbf{r} = (x(q), y(q))$, where q is the curve parameter, we find for the unit tangent vector

$$\hat{\mathbf{t}} = (x^2 + y^2)^{-1/2}(\dot{x}, \dot{y}) =: (-\sin\varphi, \cos\varphi) \tag{22}$$

where the dot denotes differentiation with respect to q. Hence we have

$$\sin\varphi = -\frac{\dot{x}}{\sqrt{(\dot{x}^2 + \dot{y}^2)}},$$

$$\cos\varphi = +\frac{\dot{y}}{\sqrt{(\dot{x}^2 + \dot{y}^2)}}. \tag{23}$$

As we are interested only in the Cartesian velocity components u and v, the tangential velocity, (19), is separated with respect to these components:

$$\frac{\partial u}{\partial t} - g\frac{\partial h}{\partial \hat{t}}\sin\varphi = 0; \quad \frac{\partial v}{\partial t} + g\frac{\partial h}{\partial \hat{t}}\cos\varphi = 0. \tag{24}$$

Using the relation

$$\frac{\partial h}{\partial \hat{t}} = -\sin\varphi\frac{\partial h}{\partial x} + \cos\varphi\frac{\partial h}{\partial y} \tag{25}$$

results in the following equations for boundary points:

$$\frac{\partial u}{\partial t} + g\sin\varphi\left(\sin\varphi\frac{\partial h}{\partial x} - \cos\varphi\frac{\partial h}{\partial y}\right) = 0,$$

$$\frac{\partial v}{\partial t} - g\cos\varphi\left(\sin\varphi\frac{\partial h}{\partial x} - \cos\varphi\frac{\partial h}{\partial y}\right) = 0. \tag{26}$$

For the transformation of equations (26) onto the computational plane the non-conservative form of the first derivatives (10), is used. Inserting these expressions into equation (26), gives the final form of the equations valid for the upper and lower sides of the rectangle (in this simple

geometry), which form the solid boundary in the transformed plane:

$$\frac{\partial u}{\partial t} + \frac{g \sin \varphi}{\sqrt{g}} \{ + \sin \varphi(h_\xi y_\eta - h_\eta y_\xi) - \cos \varphi(h_\eta x_\xi - h_\xi x_\eta) \} = 0,$$

$$\frac{\partial v}{\partial t} + \frac{g \cos \varphi}{\sqrt{g}} \{ - \sin \varphi(h_\xi y_\eta - h_\eta y_\xi) + \cos \varphi(h_\eta x_\xi - h_\xi x_\eta) \} = 0. \tag{27}$$

Let N and M be the number of points in ξ and η directions, respectively, then the transformed velocity equations (13) and (14) are valid for $\xi = 1(1)N$; $\eta = 2(1)M - 1$ (for the ring geometry) whereas the equation for the surface elevation holds for all grid points. The equations derived from the boundary conditions, (22), hold for $\xi = 1(1)N$; $\eta = 1$; M. Since we have an equidistant mesh in the transformed plane with grid spacings $\Delta\xi = \Delta\eta = 1$, the ranges of the co-ordinates ξ and η correspond to the number of grid points in each direction. No physical boundary conditions are specified along the re-entrant boundaries (resulting from the two sides of a branch cut and thus not physical boundaries) which form the left and right sides of the rectangle in the transformed plane. Rather we have the following correspondence between re-entrant grid points (periodic boundary conditions): values on $\xi = N$ correspond to those on $\xi = 1$ and values on $\xi = 0$ correspond to those on $\xi = N - 1$.

NUMERICAL SCHEME FOR THE TRANSFORMED SHALLOW WATER EQUATIONS

For the numerical solution of the system of coupled equations, (12)–(14), two staggered meshes are used; one for the components u, v and the other for h. The meshes are chosen such that velocity components are calculated on the boundary. No calculations have been performed where all three variables are computed at the same grid points. The staggered grids are depicted in Figure 3. The vertices at the squares are taken as grid points for u and v, marked by crosses, whereas the dots at the centres of the squares represent grid points for h. This grid is advantageous for strong Coriolis forces but allows decoupling[19] because interpolation is necessary to determine fluxes across cell sides. In general a marker-and-cell (MAC) type grid should be preferred[20] with surface elevation defined at the cell centre and velocities defined at mid-points of cell sides. Since for this paper several examples with Coriolis coefficients were calculated, the MAC type grid was not used. No accuracy problems were observed with our staggered grid for the present calculations.

Since the metric coefficients must be known at each vertex of a solid or dashed grid line, it is necessary that the boundary fitted grid, representing this feature, has $(2N - 1) \times (2M - 1)$ grid
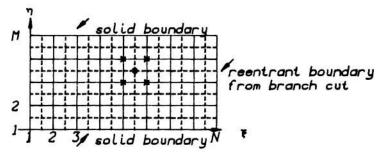

Figure 3. Crosses denote grid points for u, v and dots indicate those for h
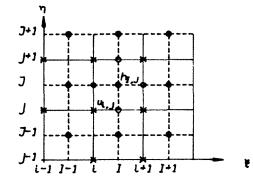
Figure 4. u, v and h have to be interpolated at points denoted by open circles

points. In Figure 4 the two sets of indices for the staggered grids are shown, where i, j denote positions for u, v and I, J denote those of h.

In order to satisfy the zero normal flow condition for solid walls, the u and v grid points are placed on the lower and upper boundaries (Figure 3).

For the numerical solution the resulting mathematical system of weakly coupled, ordinary differential equations is integrated in time by Euler's method (or by some Runge–Kutta scheme[21]) limiting the time step by the phase velocity $\sqrt{(gH)}$. If additional transport equations must be solved, flux correction techniques for general curvilinear co-ordinates could be used.

The discretized equations take the form

$$\frac{\partial h_{I,J}}{\partial t} = -\frac{1}{(\sqrt{g})_{I,J}}\{ + y_{\eta I,J}[(uH)_{i+1,J} - (uH)_{i,J}] - x_{\eta I,J}[(vH)_{i+1,J} - (vH)_{i,J}]$$

$$+ x_{\xi I,J}[(vH)_{I,j+1} - (vH)_{I,j}] - y_{\xi I,J}[(uH)_{I,j+1} - (uH)_{I,j}]\}, \tag{28}$$

$$\frac{\partial(uH)_{i,j}}{\partial t} = -\frac{gH_{i,j}}{(\sqrt{g})_{i,j}}\{ + y_{\eta i,j}[h_{I,j} - h_{I-1,j}] - y_{\xi i,j}[h_{i,J} - h_{i,J-1}]\} + (fHv)_{i,j}, \tag{29}$$

$$\frac{\partial(vH)_{i,j}}{\partial t} = -\frac{gH_{i,j}}{(\sqrt{g})_{i,j}}\{ + x_{\xi i,j}[h_{i,J} - h_{i,J-1}] - x_{\eta i,j}[h_{I,j} - h_{I-1,j}]\} - (fHu)_{i,j}. \tag{30}$$

For the boundary conditions one obtains

$$\frac{\partial(uH)_{i,j}}{\partial t} = -\frac{g(H\sin\varphi)_{i,j}}{(\sqrt{g})_{i,j}}\{ + \sin\varphi_{i,j}(y_{\eta i,j}[h_{I,j} - h_{I-1,j}] - y_{\xi i,j}[h_{i,J} - h_{i,J-1}])$$

$$+ \cos\varphi_{i,j}(x_{\eta i,j}[h_{I,j} - h_{I-1,j}] - x_{\xi i,j}[h_{i,J} - h_{i,J-1}])\}, \tag{31}$$

$$\frac{\partial(vH)_{i,j}}{\partial t} = -\frac{g(H\cos\varphi)_{i,j}}{(\sqrt{g})_{i,j}}\{ + \sin\varphi_{i,j}(-y_{\eta i,j}[h_{I,j} - h_{I-1,j}] + y_{\xi i,j}[h_{i,J} - h_{i,J-1}])$$

$$+ \cos\varphi_{i,j}(-x_{\eta i,j}[h_{I,j} - h_{I-1,j}] + x_{\xi i,j}[h_{i,J} - h_{i,J-1}])\}, \tag{32}$$

From equations (28)–(32) it is seen that u, v and h values are needed at locations which are not grid points. For the continuity equation, velocity values are needed at points $i + 1, J$; i, J; $I, j + 1$ and I, j. These values are obtained from linear interpolation in the transformed plane (in a general model this interpolation should be replaced by a weighted interpolation with the respective square roots of the metric coefficients):

$$u_{i+1,J} = \tfrac{1}{2}(u_{i+1,j} + u_{i+1,j+1}); \quad v_{I,j+1} = \tfrac{1}{2}(v_{i,j+1} + v_{i+1,j+1}). \tag{33}$$

Since the partial derivatives x_ξ, x_η, y_ξ, y_η and $\sqrt{g}$ are known on the fine grid (formed by both dashed and solid lines, see Figure 3), no interpolation is necessary for these terms. As H is a known function of x and y, all value of H can be calculated on the fine grid, prior to the beginning of the numerical calculations. For the momentum equations values for h are needed at points I,j; $I-1,j$; i,j and $i,J-1$. Again linear interpolation is used. For solid boundaries, values for h are not needed, since a staggered grid and an explicit time integration scheme for the surface elevation are used.
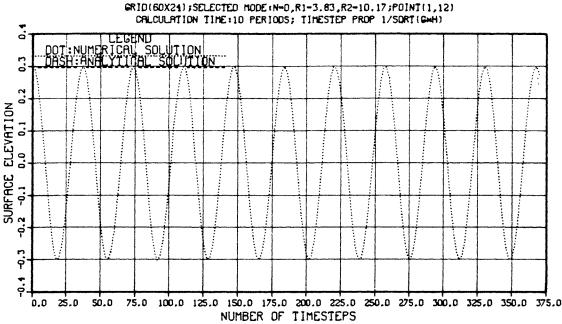
Let k,l denote the indices of a quantity on the fine grid (dimension $2N-1 \times 2M-1$), the relation between the indices of the staggered grids and those of the fine mesh are given by
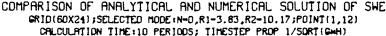
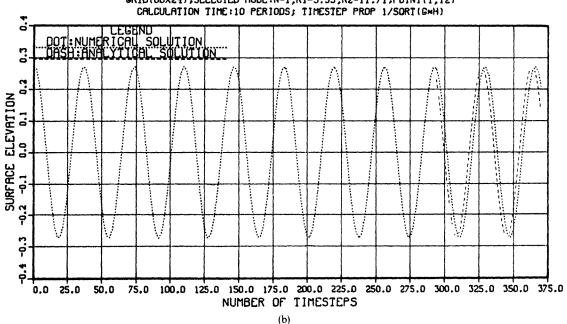$$k = 2I; \quad l = 2J; \quad k = 2i - 1; \quad l = 2j - 1. \tag{34}$$

If, for example, $(y_\eta)_{i+1,J}$ has to be determined for the continuity equation, the element $(y_\eta)_{2i+1,2J}$ of the fine grid is used. Furthermore, because of the re-entrant boundaries, fictitious grid points for elevation h are needed for $I = 0$ and $I = N$.

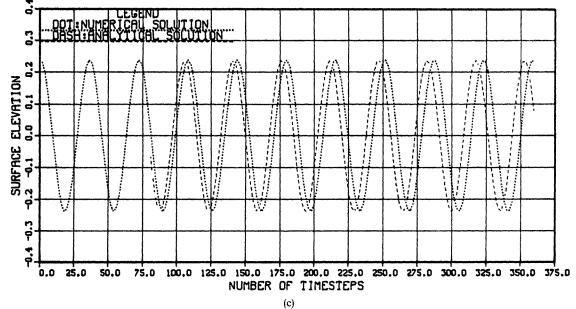## NUMERICAL RESULTS FOR NORMAL MODE SIMULATIONS

Numerical results for constant still water depth H are depicted in Figures 5–8. For actual computations, the finite difference scheme of the previous section with the non-conservative discretization for the first derivative was used. Comparisons of the non-conservative and conservative schemes showed that the latter gave rise to an oscillatory numerical error, which was substantially larger than the one obtained from the non-conservative scheme (Figure 8). When the conservative scheme is employed in the case of a plane surface ($h = $ constant), the time derivative for, e.g., u, is different from zero, owing to the existence of the term $(gH/\sqrt{g})h((y_\eta)_\xi - (y_\xi)_\eta)$, because second

COMPARISON OF ANALYTICAL AND NUMERICAL SOLUTION OF SWE
GRID(60X24);SELECTED MODE:N=0,R1=3.83,R2=10.17;POINT(1,12)
CALCULATION TIME:10 PERIODS; TIMESTEP PROP 1/SQRT(G*H)

LEGEND
DOT:NUMERICAL SOLUTION
DASH:ANALYTICAL SOLUTION

(a)

COMPARISON OF ANALYTICAL AND NUMERICAL SOLUTION OF SWE
GRID(60X24);SELECTED MODE:N-1,R1-5.33,R2-11.71;POINT(1,12)
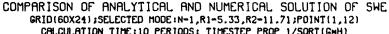CALCULATION TIME:10 PERIODS; TIMESTEP PROP 1/SQRT(G*H)

(b)

COMPARISON OF ANALYTICAL AND NUMERICAL SOLUTION OF SWE
GRID(60X24);SELECTED MODE:N-3,R1-8.02,R2-14.59;POINT(1,12)
CALCULATION TIME:10 PERIODS; TIMESTEP PROP 1/SQRT(G*H)

(c)

COMPARISON OF ANALYTICAL AND NUMERICAL SOLUTION OF SWE
GRID(90X12);SELECTED MODE:N-4,R1-9.28,R2-15.96;POINT(1,6)
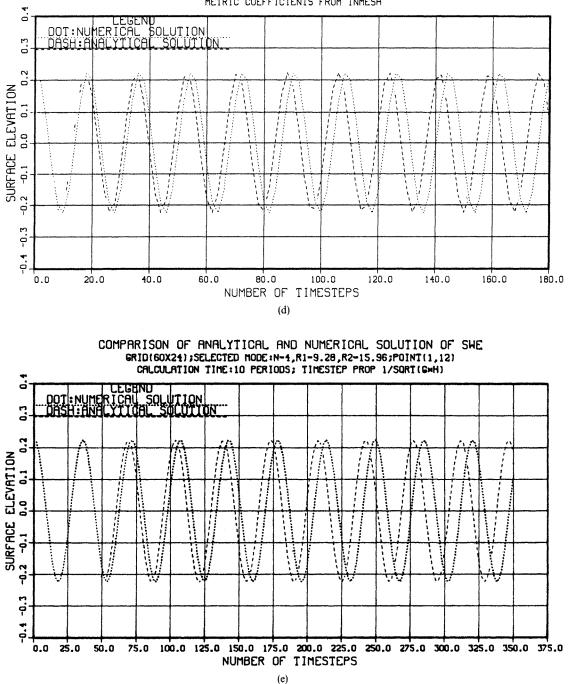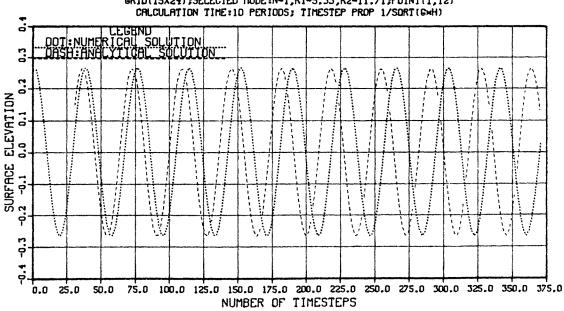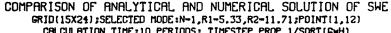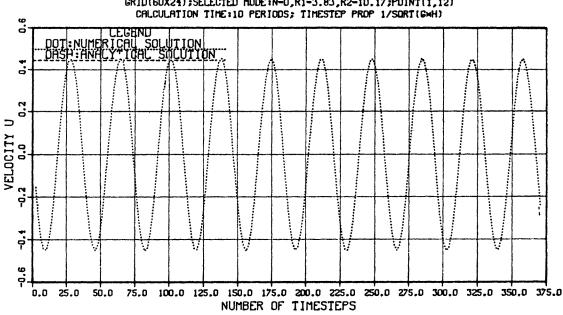METRIC COEFFICIENTS FROM INMESH

(d)

COMPARISON OF ANALYTICAL AND NUMERICAL SOLUTION OF SWE
GRID(60X24);SELECTED MODE:N-4,R1-9.28,R2-15.96;POINT(1,12)
CALCULATION TIME:10 PERIODS; TIMESTEP PROP 1/SQRT(G*H)

(e)

Figure 5. Figures (a)–(e) show a comparison between analytic and numerical solutions of surface elevation for modes $n = 0$ to $n = 4$ at grid point $I = 1, J = 12$. Since higher modes (increasing n) exhibit more structure, the number of grid points per wavelength is reduced, and hence deviations from the analytic solution occur at earlier times
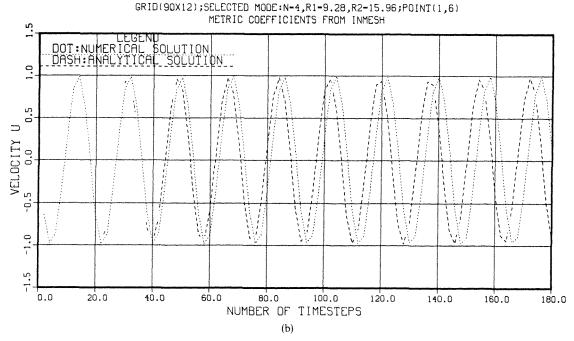
COMPARISON OF ANALYTICAL AND NUMERICAL SOLUTION OF SWE
GRID(15X24);SELECTED MODE:N-1,R1-5.33,R2-11.71;POINT(1,12)
CALCULATION TIME:10 PERIODS; TIMESTEP PROP 1/SQRT(G*H)

Figure 6. If the number of grid points is reduced to 15×24, the solution for $n = 1$ shows the same behaviour as for $n = 4$ on a 60×24 grid, indicating that accuracy depends on the number of grid points per wavelength

COMPARISON OF ANALYTICAL AND NUMERICAL SOLUTION OF SWE
GRID(60X24);SELECTED MODE:N-0,R1-3.83,R2-10.17;POINT(1,12)
CALCULATION TIME:10 PERIODS; TIMESTEP PROP 1/SQRT(G*H)

(a)

COMPARISON OF ANALYTICAL AND NUMERICAL SOLUTION OF SWE
GRID(90X12);SELECTED MODE:N-4,R1-9.28,R2-15.96;POINT(1,6)
METRIC COEFFICIENTS FROM INMESH

(b)

Figures 7(a) 7(b) The u-velocity (same with v-component) is depicted for modes $n = 0$ and $n = 4$. For modes $n = 1$ to $n = 3$ the same behaviour as for surface elevation is observed. The v-component at grid point (1, 12) is equal to zero

NUMERICAL ERROR IN SOLUTION OF THE SHALLOW WATER EQUATIONS
GRID(60X24);H-CONST-10.;V-VPHI;POINT(1,1)
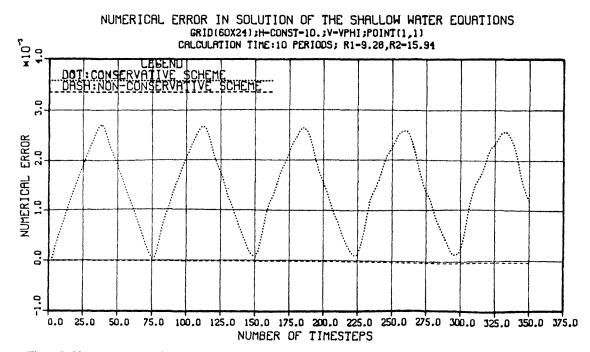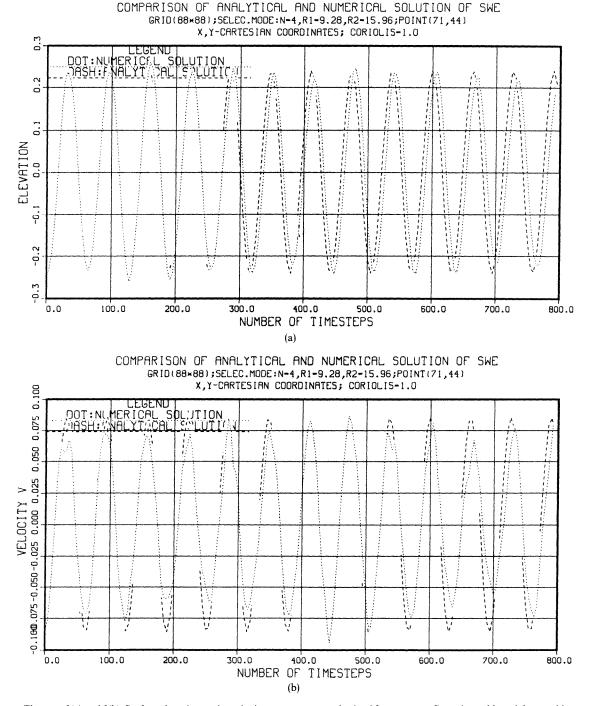CALCULATION TIME:10 PERIODS; R1-9.28,R2-15.94

Figure 8. Numerical errors for constant water depth D, resulting from both conservative and non-conservative discretizations of first derivatives are shown. The conservative scheme exhibits much larger and oscillating numerical errors when compared with those of the non-conservative discretization. The numerical error for the conservative scheme is proportional to surface elevation h whereas the error for the non-conservative one is independent of h

COMPARISON OF ANALYTICAL AND NUMERICAL SOLUTION OF SWE
GRID(88×88);SELEC.MODE:N-4,R1-9.28,R2-15.96;POINT(71,44)
X,Y-CARTESIAN COORDINATES; CORIOLIS-1.0

(a)

COMPARISON OF ANALYTICAL AND NUMERICAL SOLUTION OF SWE
GRID(88×88);SELEC.MODE:N-4,R1-9.28,R2-15.96;POINT(71,44)
X,Y-CARTESIAN COORDINATES; CORIOLIS-1.0

(b)

Figures   9(a) and 9(b). Surface elevation and v-velocity component as obtained from an x–y Cartesian grid model at a grid point near the inner radius of the annular ring are depicted. In this model the boundary was represented in a step fashion resulting in a very fine grid (88 × 88) to sufficiently resolve geometrical details. This corresponds to some 170 points along the inner circumference and to about 300 points for the outer circumference. In general, the solution produced by this model was good except at grid points near boundaries where the calculations of the flow field were inaccurate

COMPARISON OF ANALYTICAL AND NUMERICAL SOLUTION OF SWE
GRID(88×88);SELEC.MODE:N-4,R1-9.28,R2-15.96;POINT(85,44)
X,Y-CARTESIAN COORDINATES; CORIOLIS-1.0

(a)

COMPARISON OF ANALYTICAL AND NUMERICAL SOLUTION OF SWE
GRID(88×88);SELEC.MODE:N-4,R1-9.28,R2-15.96;POINT(85,44)
X,Y-CARTESIAN COORDINATES; CORIOLIS-1.0

(b)

Figures 10(a) and (b). Surface elevation and v-velocity component as obtained from an $x-y$ Cartesian grid model at a grid point near the outer radius of the annular ring are shown. Again, inaccuracies of the surface elevation and the velcoity are produced. This may lead to gross errors in the calculation of passive transport in the vicinity of curved boundaries (e.g. thermal plume calculation in harbour areas, see Figure 1). Owing to the large number of grid points, the computation time of this model is a factor three higher than for the BFG model

derivatives do not cancel numerically. Hence, this term provides a numerical source of energy. Therefore, the non-conservative form was preferred.

In general, numerical simulations were performed on a 60×24 grid; i.e. 60 grid points in the azimuthal and 24 in the radial direction were used, which demanded a boundary fitted grid of size 119×47. It was, however, found that the same accuracy (or better) was obtained with a 90×12 grid or even a 60×12 grid was sufficient. It can be shown, and was confirmed by computations, that the accuracy of the numerical solution only depends on the number of grid points per wavelength.

The influence of this number on the accuracy is demonstrated in Figure 6, where a 15×24 grid was used for $n = 1$, which corresponds to a 60×24 grid for mode $n = 4$. Since the frequency, that is the number of zeros in azimuthal direction, is proportional to n, the number of grid points per wavelength diminishes with increasing radial mode number, and hence accuracy is reduced. Velocities are depicted in Figure 7(a) and 7(b), and show the same accuracy behaviour as surface elevation.

In most cases it will be advantageous to obtain solutions in contravariant components (i.e. v^ξ and v^η) in order to locally rotate the co-ordinate system in the flow direction and hence reduce numerical diffusion. Moreover, the formulation of boundary conditions is facilitated. For the present case, however, this is an advantage for $n = 0$ only. Since a stability analysis for the transformed shallow water equations has not yet been performed, the finite difference contours of a circular basin for a uniform triangular grid were used[8] to estimate the number of necessary grid points in the ξ and η directions. Using Thacker's results[8] shows that frequencies are well approximated for waves larger than four grid spacings; i.e. $k\Delta < \pi/2$. Since in the physical plane grid spacings vary in the r-direction, this demands that $N > 4R_m$ and $M > 2/\pi R_m$ where R_m is the mean of the inner and outer radii of the circular ring basin. This is a lower limit since the above stability condition is reached only for the maximal time step. Since an irregular grid is used, no optimal time step exists. Hence the number of grid points is doubled in each direction. If a basin with parabolic depth profile or any other profile is simulated, an optimal time step does not exist for a regular grid either. Since in practical applications depth variations occur, the use of regular grids does not give an advantage. In Figures 9 and 10 the results of an x–y Cartesian grid model are presented. In this model the boundary was approximated as a step function, and a rectangular uniform grid was used. The number of grid points was 88×88 in order to resolve geometrical details. In general, the solution produced by this model was good, except at grid points near the inner and outer circumferences where the flow field was inaccurately modelled. Because of the high number of grid points, computer time was a factor three higher than for the BFG model. Furthermore, it is assumed that the accuracy of the Cartesian grid model deteriorates when variable coefficients (H not constant) are used. For the BFG model variable coefficients are produced by varying metric components even if H is constant.

CONCLUSIONS AND OUTLOOK

The solution of the SWEs on a circular ring provides a particularly good basis for the testing of boundary fitted co-ordinate systems, since comparisons with the analytic solution for both velocity components and surface elevation are possible. Moreover, frequencies of the normal mode simulations can be checked too.

All calculations were performed on a uniform grid in the transformed plane, and no instabilities (in one example some 1000 periods were calculated) were found which could have been expected from the variable coefficients generated by the transformation. The numerical scheme remained stable even for Coriolis parameter $f = 1$.

Analytic solutions also exist for a circular ring basin with parabolic depth profile $H = H_0(1 - r^2/R^2)$. No calculations have been performed for this case. Furthermore, the influence of grid line concentration on accuracy and stability has not been investigated. Several other numerical schemes are possible, e.g. if transport equations are solved it may be advantageous to resort to flux-corrected transport techniques.

The approximation of the first spatial derivatives is of great importance since the use of a conservative form may lead to inaccuracies, because second derivatives do not cancel in general. Even for constant h, terms proportional to $h(y_{\xi\eta} - y_{\eta\xi})$ etc. occur, which provide a numerical source of energy. Most likely these terms will not cause stability problems in parabolic equations where sufficient damping exists, but may cause oscillations in hyperbolic systems. However, the accuracy of the solution will be affected in both cases.

It has been demonstrated that BFGs are useful for problems with curving boundaries, which occur in many cases of practical interest. Further investigations are necessary concerning the stability of the transformed equations. Particular attention should be given to the influence of the co-ordinate system used for the numerical simulation. In this paper the same results were obtained for metric coefficients determined from polar co-ordinates and for those determined from a grid point distribution resulting from the solution of Laplace's equation. Problems with known analytic solutions (linear and non-linear) on complex solution domains will be most useful for the comparison with numerical results, e.g. Reference 22.

In addition, numerical results from a conventional model (x, y–Cartesian co-ordinates) were presented where the boundary is represented in a step fashion. Although a much finer grid is used (88×88), there a grid points near the inner and outer radii of the annular ring where, in contrast to the behaviour of the solution in the interior, surface elevation and velocity elevation are not accurately approximated. This gives a hint that in situations where simulations near curved boundaries are important (e.g. harbour area (see Figure 1) or for complicated bottom topography) such a model may lead to incorrect results.

Furthermore, the computation time of the BFG model was only one third of that of the Cartesian grid model, showing that there are cases were BFG models are more economical. It is expected that in cases of practical applications the accuracy of the Cartesian grid model will decrease further, since in the example of the annular ring only constant coefficients (constant depth) were used, whereas in the BFG model variable coefficients, due to the transformation, were already employed.

REFERENCES

1. W. C. Thacker, 'Irregular grid finite-difference techniques simulations of oscillations in shallow circular basins', *J. Phys. Ocean.*, **7**, 282–292 (1977).
2. N. Praagman, 'Numerical solution of the shallow water equations by a finite element method', *Dissertation*, T. H. Delft, 1979.
3. C. Cuvelier *et al.*, *A Survey of Finite Element Methods in Fluid Mechanics*, T. H. Delft, 1979.
4. R. H. Gallagher *et al.*, *Finite Elements in Fluids*, Wiley, 1982.
5. K. P. Holz *et al.*, 'Verifikation eines numerischen Tidemodells', *Wasserwirtschaft*, **71**, (10), 289–294 (1981).
6. C. Taylor, '*Finite Element Programming of the Navier–Stokes Equations*, Pineridge Press, Swansea, 1981.
7. W. C. Thacker, 'Comparison of finite element and finite difference schemes. Part 1: one-dimensional gravity wave motion', *J. Ocean.*, **8**, 676–679 (1978).

8. W. C. Thacker, 'Comparison of finite element and finite difference schemes. Part 2: two-dimensional gravity wave motion', *J. Ocean.*, **8**, 680–689 (1978).
9. J. F. Thompson *et al.*, 'Automatical numerical generation of body-fitted curvilinear coordinate system for field containing any number of arbitrary two-dimensional bodies', *J. Comp. Phys.*, **15**, 299–319 (1974).
10. J. F. Thompson, 'WESCOR—boundary fitted coordinate code for general 2D regions with obstacles and boundary intrusions', *ARO Report 82-3*, 1982.
11. J. F. Thompson, 'General curvilinear coordinate systems', in J. F. Thompson (ed.), *Numerical Grid Generation*, North-Holland 1982, pp. 2–30.
12. J. F. Thompson, 'Elliptic grid generation', in J. F. Thompson (ed.), *Numerical Grid Generation*, North-Holland, 1982, pp. 79–106.
13. J. F. Thompson, 'A boundary fitted coordinate code for general two-dimensional regions with obstacles and boundary intrusions; environmental and water quality operational studies', *Technical Report E-83-8*, 1983.
14. B. H. Johnson, 'Numerical modeling of estuaries hydrodynamics on a boundary fitted coordinate system', in J. F. Thompson (ed.) *Numerical Grid Generation*, North Holland, 1982, pp. 409–436.
15. R. M. Coleman, 'Generation of a boundary fitted coordinate system using segmented computational region', in J. F. Thompson (ed.) *Numerical Grid Generation*, North Holland, 1982, pp. 633–652.
16. W. C. Mastin, 'Error induced by coordinate systems', in J. F. Thompson (ed.) *Numerical Grid Generation*, North Holland, 1982, pp. 31–40.
17. G. D. Kerlick, 'Assessing the quality of curvilinear coordinate meshes by decomposing the Jacobian matrix', in J. F. Thompson (ed.) *Numerical Grid Generation*, North Holland. 1982, pp. 787–807.
18. H. Lamb, *Hydrodynamics*, 6th Edition, Dover, New York, 1945.
19. R. S. Bernard, 'Grid implementation for incompressible flow', *Lecture Notes of the Short Course on Numerical Grid Generation*, Mississippi State University, 11–15 June 1984.
20. F. Mesinger and A. Arakawa, *Numerical Methods Used in Atmospheric Models, Volume 1*, GARP Publications, Series No. 17, 1976.
21. S. T. Zalesak, 'Fully multidimensional flux corrected transport algorithms for fluids', *J. of Comp. Phys.* **31**, 335–362 (1979).
22. W. C. Thacker, 'Some exact solutions of the nonlinear shallow-water wave equations', *J. Fluid Mechanics*, **107**, 499–508 (1981).
23. D. L. Book, *et al. Finite Difference Techniques for Vectorized Fluid Dynamics Calculations*, Springer, Berlin, 1981.